Electronic Supplementary Information

Highly Efficient N_2 Fixation Catalysts: Transition-metal Carbides M_2C (MXenes)

Shuo Wang,[#,a] Bo Li,[#,c] Ziqi Tian,[a,b] Lei Li,[a] and Qiuju Zhang,*[,a,b] Liang Chen,*[,a,b] Xiao Cheng Zeng*[,d]

[a] Ningbo Institute of Materials Technology and Engineering, Chinese Academy of Sciences, Ningbo, Zhejiang 315201, China

[b] University of Chinese Academy of Sciences, Beijing, 100049, China

[c] Department of Chemistry, University of California Riverside, California 92521, United States

[d] Department of Chemistry, University of Nebraska-Lincoln Lincoln, NE, 68588, USA

NRR Mechanism

Six proton and electron transfer steps are involved in the cathode reaction in the electrochemical process of producing NH_3, as written in (1):

$$N_2 + 6H^+ + 6e^- \rightarrow 2NH_3 \quad (1)$$

Possible intermediates in each reaction step formed are N_2H_x or NH_x species. Here, the NRR reactions in the distal and alternating mechanisms are investigated, based on the known reaction elementary steps proposed by Nørskov.[1] The calculated reaction free energy of NH_3 formation in the gas phase is taken from a previous work[2] (see Table S3 where values from other groups are also cited). The enzymatic mechanism can undergo two possible NH_3 desorption paths, *i.e.* our proposed “step-by-step” NH_3 desorption and the well-known final desorption of two NH_3, denoted as (a) and (b) in the following equations. The initial N_2 adsorption structure is side-on model where two asterisk (2*) denotes the two hollow sites (H1 and H2) for the adsorption on the surface.

$$2^* + N_2 \rightarrow {}^*N\text{-}{}^*N \quad (2)$$

$$^*N\text{-}{}^*N + H^+ + e^- \rightarrow {}^*N\text{-}{}^*NH \quad (3)$$

$$^*N\text{-}{}^*NH + H^+ + e^- \rightarrow {}^*NH\text{-}{}^*NH \quad (4)$$

$$^*NH\text{-}{}^*NH + H^+ + e^- \rightarrow {}^*NH + {}^*NH_2 \quad (5a)$$

$$^*NH\text{-}{}^*NH + H^+ + e^- \rightarrow {}^*NH\text{-}{}^*NH_2 \quad (5b)$$

$$^*NH\text{-}{}^*NH_2 + H^+ + e^- \rightarrow {}^*NH + NH_3(g) \quad (6a)$$

$$^*NH\text{-}{}^*NH_2 + H^+ + e^- \rightarrow {}^*NH_2\text{-}{}^*NH_2 \quad (6b)$$

$$^*NH + H^+ + e^- \rightarrow {}^*NH_2 \quad (7a)$$

$$^*NH_2\text{-}{}^*NH_2 + H^+ + e^- \rightarrow {}^*NH_2 + {}^*NH_3 \quad (7b)$$

$$^*NH_2 + H^+ + e^- \rightarrow {}^*NH_3 \quad (8a)$$

$$^*NH_2 + {}^*NH_3 + H^+ + e^- \rightarrow {}^*NH_3 + {}^*NH_3 \quad (8b)$$

$$^*NH_3 \rightarrow NH_3(g) \quad (9a)$$

$$^*NH_3 + {}^*NH_3 \rightarrow 2NH_3\,(g) \quad (9b)$$

In the M_2C (M= Sc, Ti, V, Cr, Mn, Fe, Zr, Nb, Hf, Ta) systems considered, N-N broken occurs at the fourth H* attacking, except for Mo_2C, which occurs at the third H* addition. Equations of 5a, 6a, 7a, 8a and 9a display the “step-by-step” NH_3

desorption while the corresponding equations 5b-9b present the two NH_3 final desorption process.

Table S1 Computed lattice constants of the optimized structures for M_2C MXenes, compared with previous work.

		Previous results				Current results			
	type	a(Å)	d_{M-C}(Å)	d_{M-M}(Å)	θ	a	d_{M-C}(Å)	d_{M-M}(Å)	θ
Sc_2C	T	3.31	2.26	2.41	85.87	3.30	2.26	2.40	85.64
Ti_2C	T	3.04	2.10	2.3	87.34	3.05	2.09	2.27	86.49
V_2C	H	2.79	2.04	2.51	75.78	2.74	2.04	2.57	78.11
Cr_2C	T	2.82	1.93	2.08	86.30	2.80	1.94	2.11	87.15
Mn_2C	T	2.71	1.91	2.18	89.41	2.69	1.88	2.18	87.97
Fe_2C	T	-	-	-	-	2.80	1.91	2.05	86.10
Zr_2C	T	2.71	1.91	2.18	89.41	2.69	1.90	2.19	89.46
Nb_2C	T	3.12	2.16	2.37	87.27	3.09	2.15	2.39	87.81
Mo_2C	H	2.85	2.14	2.73	79.27	2.83	2.13	2.73	79.76
Hf_2C	T	3.21	2.15	2.73	79.27	3.19	2.24	2.54	89.08
Ta_2C	T	3.08	2.15	2.43	88.68	3.06	2.15	2.43	88.95

Table S2 Computed adsorption energies of N_2 on different M_2C MXenes and the compared onset potential of previous different catalysts for NRR.

TM	Adsorption energy (eV)		Side on onset potential (eV)	Rate-determination step (RDS)
	N_2-side on (N-N bond lengths)	N_2-end on (N-N bond lengths)		
Sc_2C	-3.20(1.35)	-0.64(1.14)	1.59	$*NH_2*NH_2+H^{-}+e^{-}\rightarrow*NH_2*NH_3$
Ti_2C	-3.34(1.35)	-0.96(1.14)	1.59	$*NH*NH+H^{-}+e^{-}\rightarrow*NH*NH_2$
V_2C	-3.40(1.32)	-0.93(1.14)	0.69	$*NH_2*NH_3+H^{-}+e^{-}\rightarrow*NH_3*NH_3$
Cr_2C	-2.59(1.29)	-1.60(1.14)	0.68	$*NH_2*NH_3+H^{-}+e^{-}\rightarrow*NH_3*NH_3$
Mn_2C	-1.42(1.27)	-1.30(1.14)	0.28	$*NH_2*NH_3+H^{-}+e^{-}\rightarrow*NH_3*NH_3$
Fe_2C	-0.43(1.24)	-0.89(1.13)	0.23	$*N_2+H^{-}+e^{-}\rightarrow*NNH$
Zr_2C	-3.08(1.36)	-0.84(1.14)	1.17	$*NH_2*NH_3+H^{-}+e^{-}\rightarrow*NH_3*NH_3$
Nb_2C	-2.71(1.36)	-1.08(1.18)	0.67	$*NH_2*NH_2+H^{-}+e^{-}\rightarrow*NH_2*NH_3$
Mo_2C	-2.04(1.29)	-1.11(1.13)	0.46	$*NH_2*NH_3+H^{-}+e^{-}\rightarrow*NH_3*NH_3$
Hf_2C	-3.24(1.20)	-0.72(1.13)	1.55	$*NH_2*NH_3+H^{-}+e^{-}\rightarrow*NH_3*NH_3$
Ta_2C	-2.48(1.39)	-1.11(1.14)	0.68	$*NH_2*NH_3+H^{-}+e^{-}\rightarrow*NH_3*NH_3$
Previous results		B/g-C_3N_4	0.20[3]	$*NH_2*NH_2+H^{-}+e^{-}\rightarrow*NH_2*NH_3$
		Ti@NVs-g-C_3N_4	0.51[4]	$*NH_2+H^{-}+e^{-}\rightarrow*NH_3$
		MoC_6	0.54[5]	$*N_2+H^{-}+e^{-}\rightarrow*N_2H$
		W@g-C_3N_4	0.25[6]	$*NH_2*NH_2+H^{-}+e^{-}\rightarrow*NH_2*NH_3$
		B-Graphene	0.31[7]	$*NH*NH_2+H^{-}+e^{-}\rightarrow*NH_2*NH_2$

Table S3 Calculated zero-point energies (ZPEs), entropy terms (TS), and free energy formation (ΔG) for gas-phase molecules and adsorbed species on Mn_2C in enzymatic reactions (eV). Asterisk (*) denotes adsorbed molecules.

Mn_2C	ZPE	TS	ΔG
$*N_2$	0.17	0.10	-0.89
*NNH	0.44	0.17	0.26
*NHNH	0.76	0.17	-1.18
$*NHNH_2$	1.08	0.12	-0.62
$*NH_2NH_2$	1.40	0.14	-0.08
$*NH_2NH_3$	1.74	0.20	0.22
$*NH_3NH_3$	2.08	0.23	0.28
$*NHNH_3$	1.34	0.17	-0.55
*NH	0.35	0.09	0.73
$*NH_2$	0.65	0.13	0.38
$*NH_3$	1.02	0.14	0.28
H_2(g)	0.27 $^{\text{our work}}$, 0.27[8] , 0.279]	0.41 $^{\text{our work}}$, 0.39[8] , 0.40[9]	
N_2(g)	0.15 $^{\text{our work}}$, 0.15[8] , 0.14[9]	0.60 $^{\text{our work}}$, 0.58[8] , 0.59[9]	-0.99 $^{\text{our work}}$, -1.27[8] , -0.79[9]
NH_3(g)	0.89 $^{\text{our work}}$, 0.58[8] , 0.85[9]	0.74 $^{\text{our work}}$, 0.56[8] , 0.60[9]	

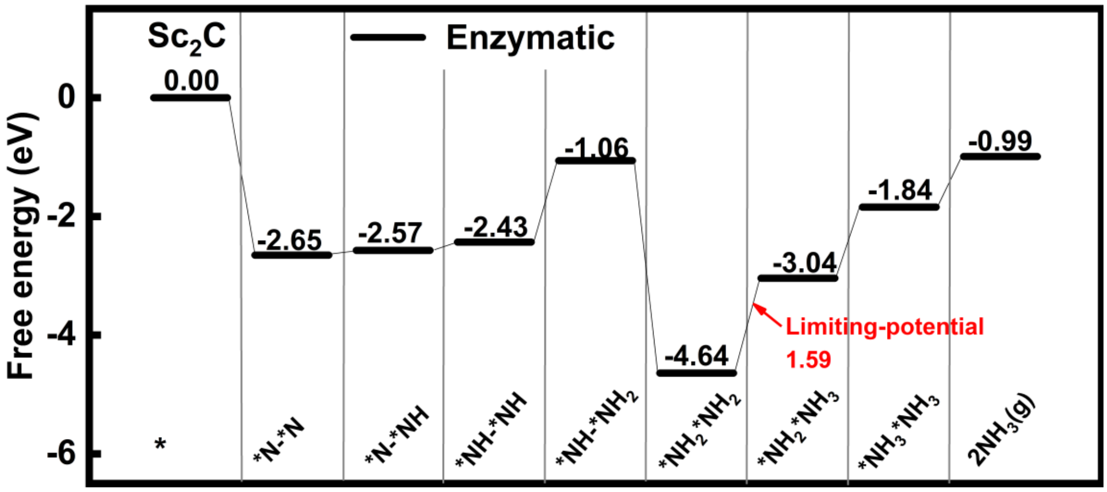

Figure S1 Free-energy diagrams in enzymatic mechanism for Sc$_2$C.

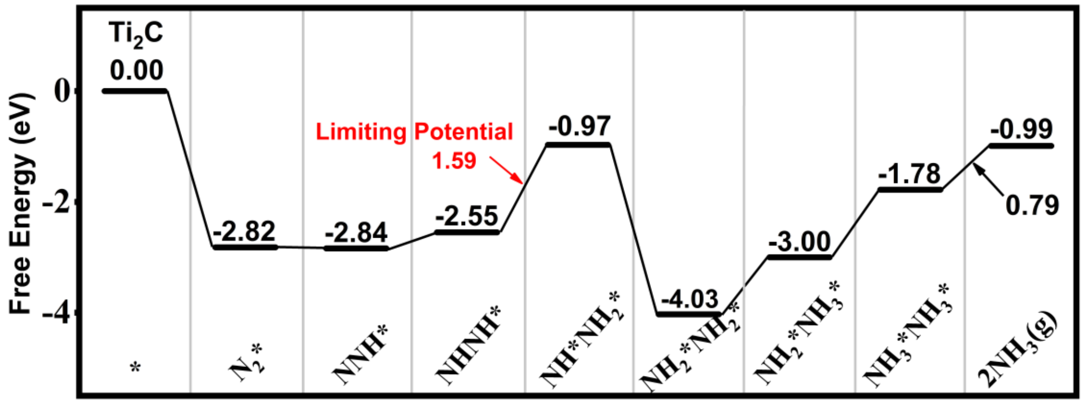

Figure S2 Free-energy diagrams in enzymatic mechanism for Ti$_2$C.

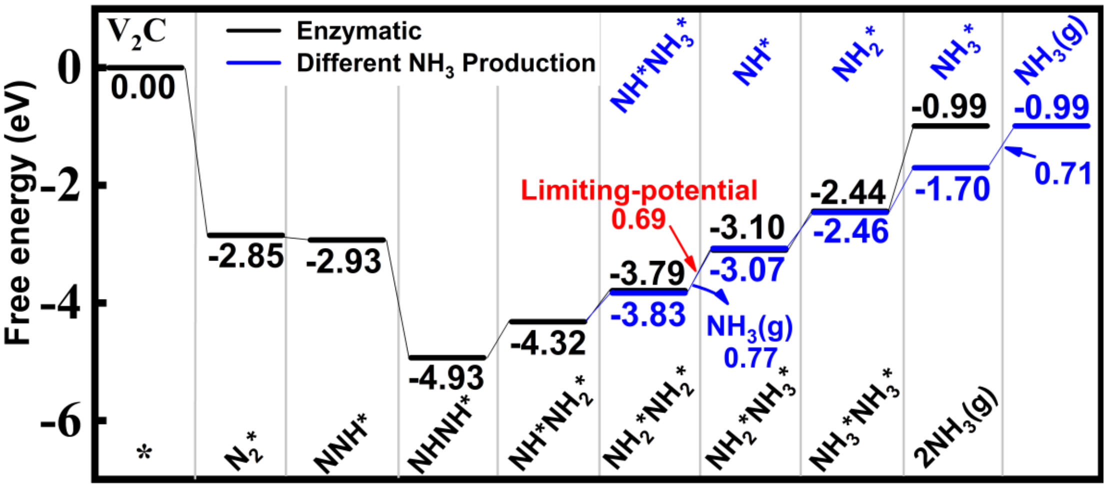

Figure S3 Free-energy diagrams for the step-by-step NRR in enzymatic mechanism for V$_2$C.

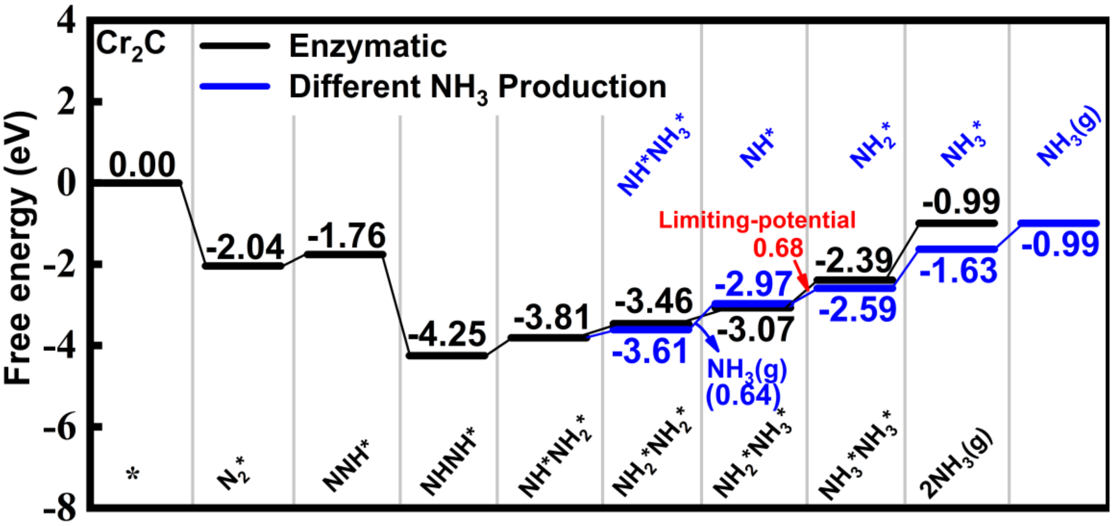

Figure S4 Free-energy diagrams for the step-by-step NRR in enzymatic mechanism for Cr$_2$C.

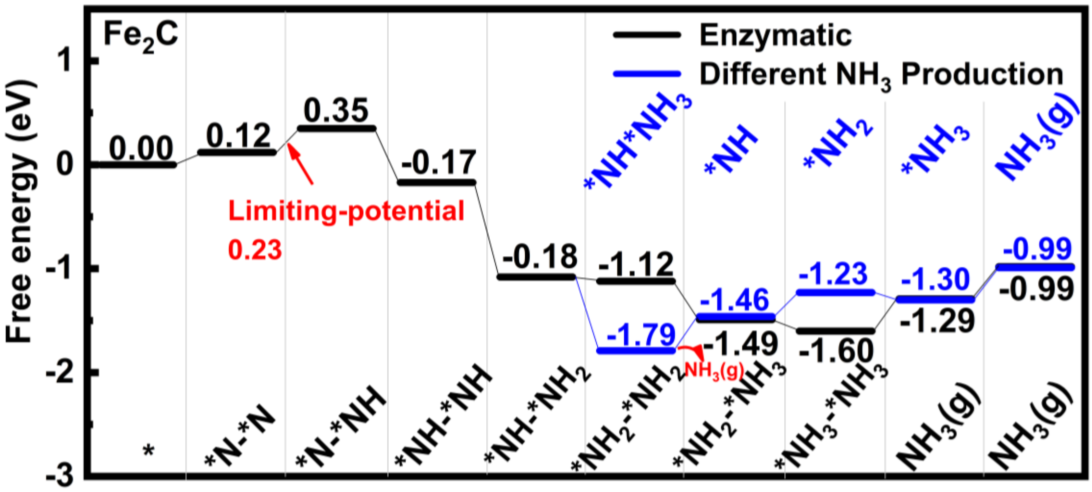

Figure S5 Free-energy diagrams for the step-by-step NRR in enzymatic mechanism for Fe$_2$C.

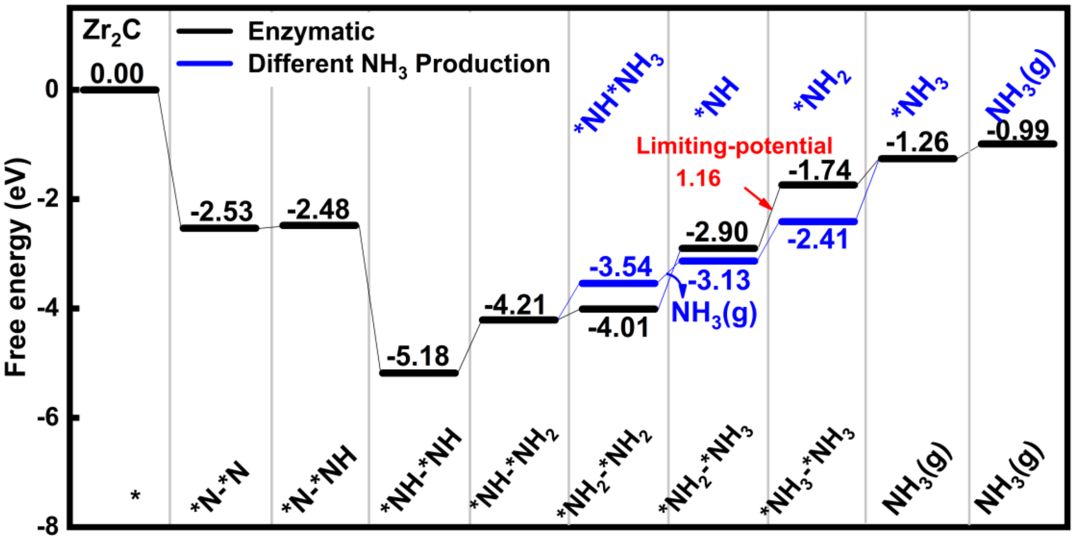

Figure S6 Free-energy diagrams in enzymatic mechanism for Zr_2C.

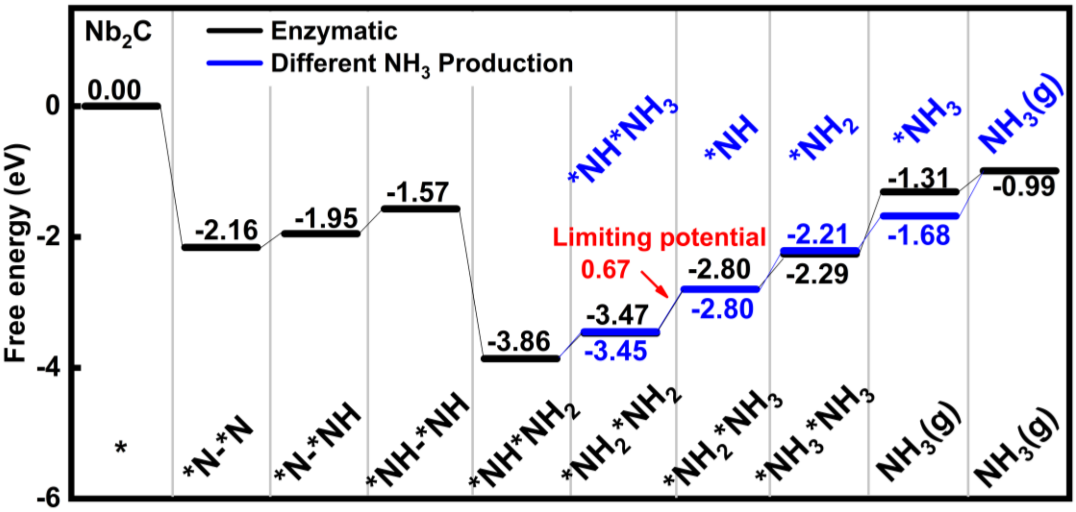

Figure S7 Free-energy diagrams for the step-by-step NRR (blue line) and both NH_3 final-desorption (black-line) in enzymatic mechanism for Nb_2C.

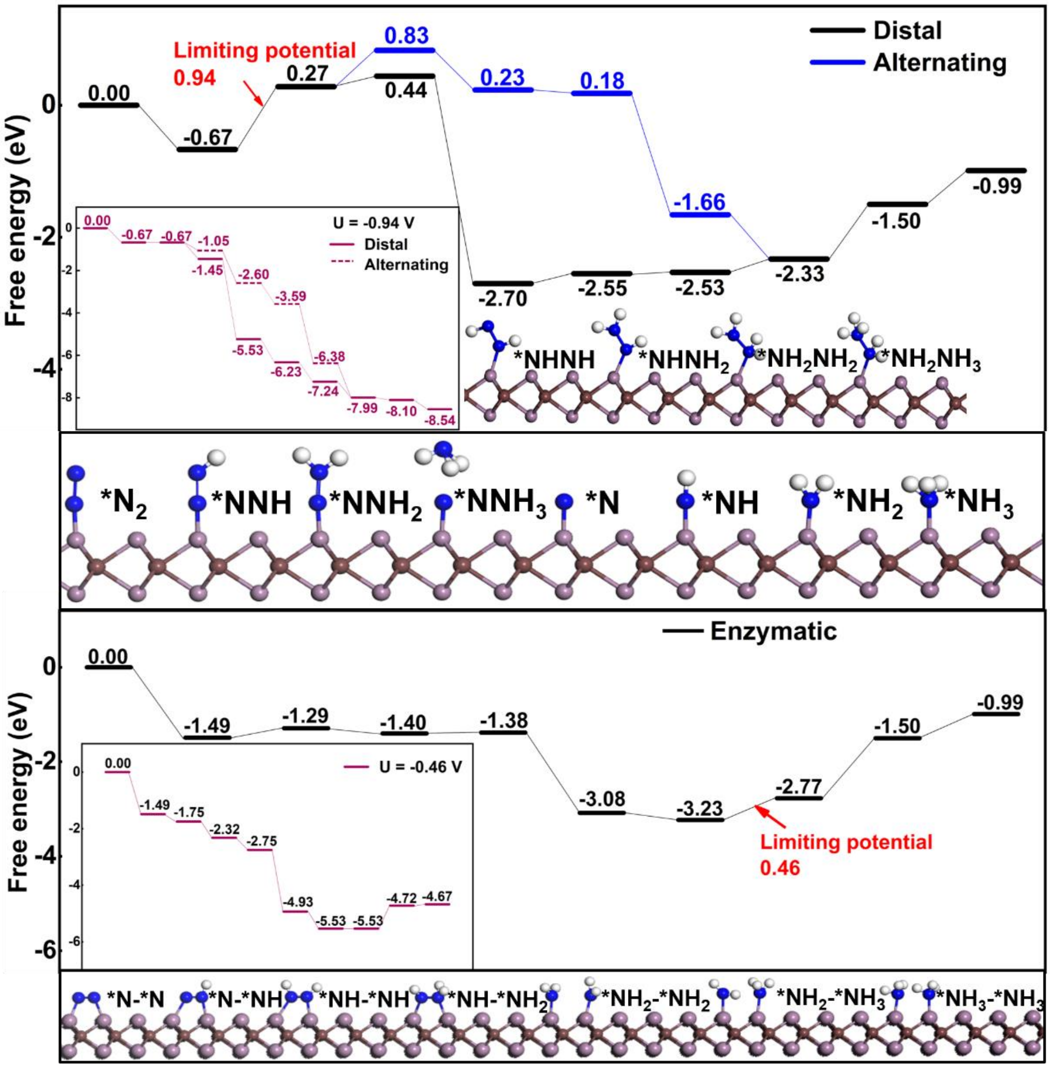

Figure S8 Free-energy diagrams for NRR in distal, alternating (top panel) and enzymatic (bottom panel) mechanism for Mo_2C.

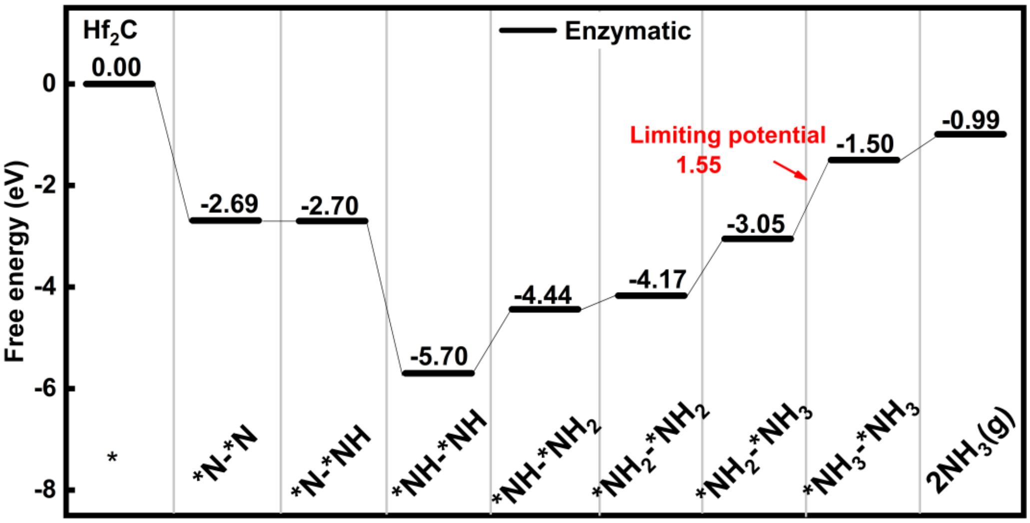

Figure S9 Free-energy diagram in enzymatic mechanism for Hf_2C.

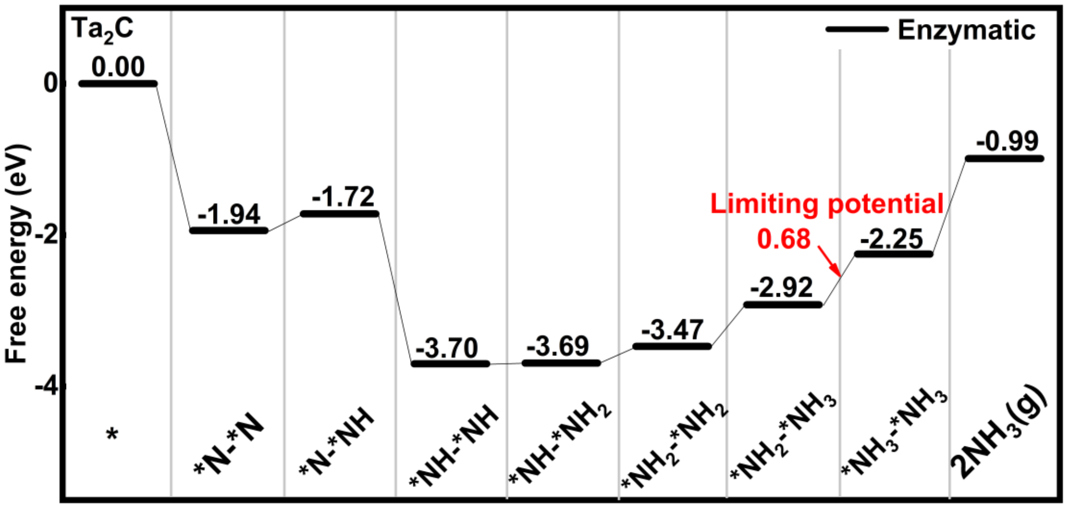

Figure S10 Free-energy diagram in enzymatic mechanism for Ta_2C.

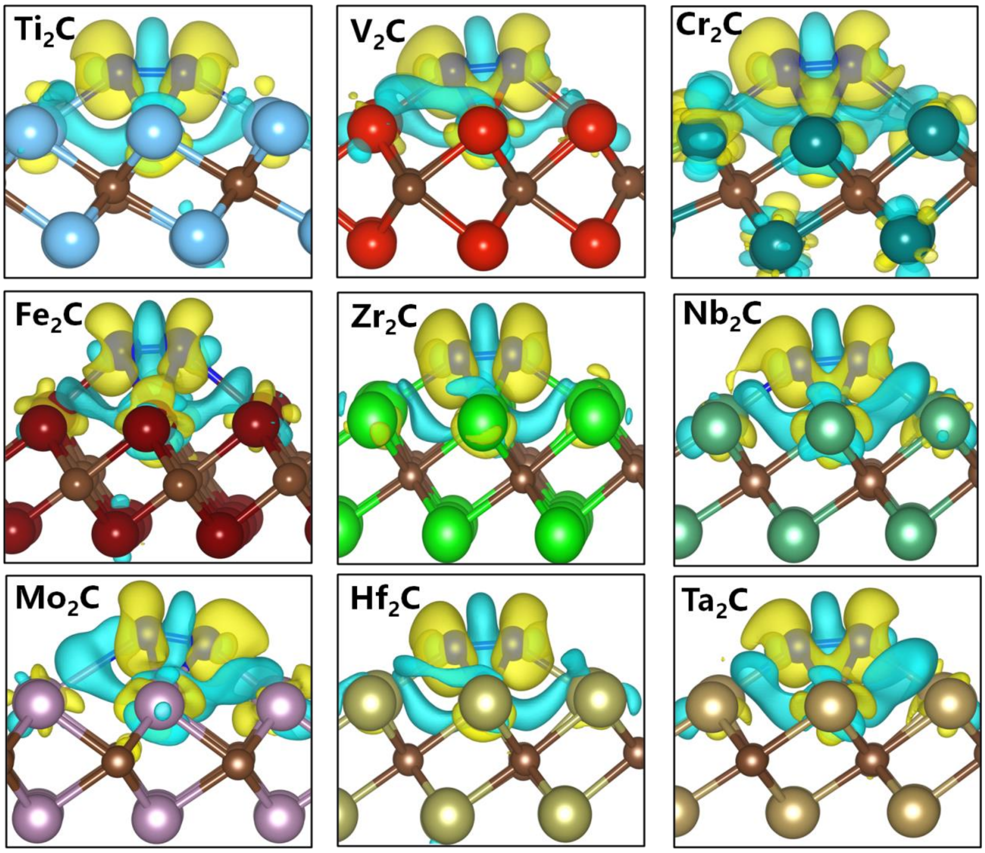

Figure S11 Charge-density differences for each M_2C system with iso-surface at 0.003 e/$Å^3$. Yellow and blue contours represent electron accumulation and depiction, respectively.

Table S4 Computed Bader charge transfer between N_2 and surface metals on M_2C MXenes.

TM	Charge gain on N_2 (e)	Charge lost on M2/M3 of M_2C-N_2 (e)	Charge lost on M2/M3 of pristine M_2C(e)	Charge transfer from M2/M3 to N_2(e)
Sc_2C	0.96	1.49	1.20	0.29
Ti_2C	0.89	1.33	1.08	0.25
V_2C	0.94	1.49	1.16	0.33
Cr_2C	0.77	1.30	1.10	0.20
Mn_2C	0.59	0.85	0.65	0.20
Fe_2C	0.53	0.88	0.72	0.16
Zr_2C	0.91	1.43	1.07	0.36
Nb_2C	0.83	1.24	0.90	0.34
Mo_2C	0.80	1.16	0.93	0.23
Hf_2C	1.00	1.64	1.21	0.43
Ta_2C	0.92	1.41	1.05	0.36

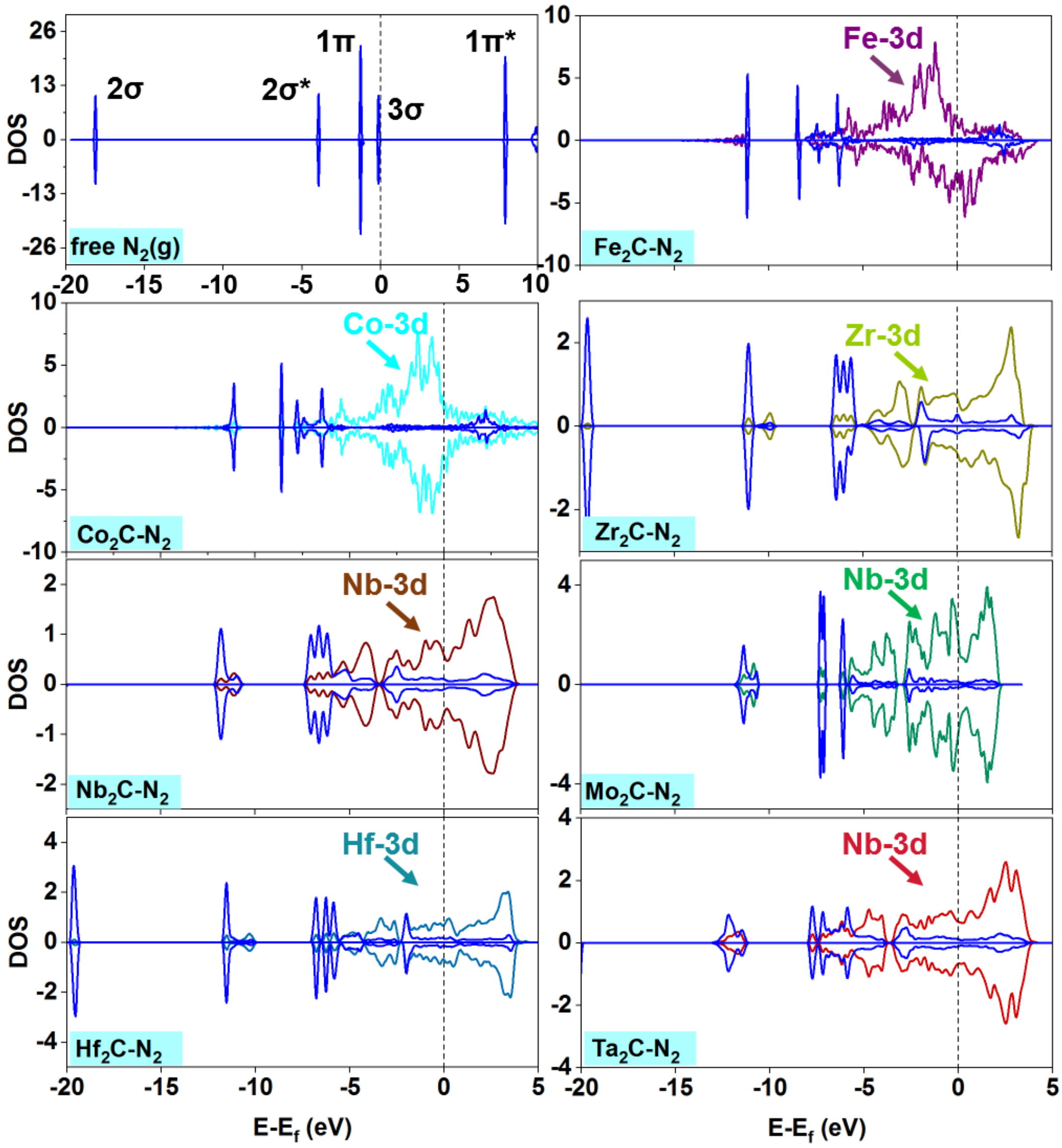

Figure S12 Computed spin-polarized local density of state (LDOS) of free N_2 molecule and N_2 side-on adsorption structures on each M_2C MXenes.

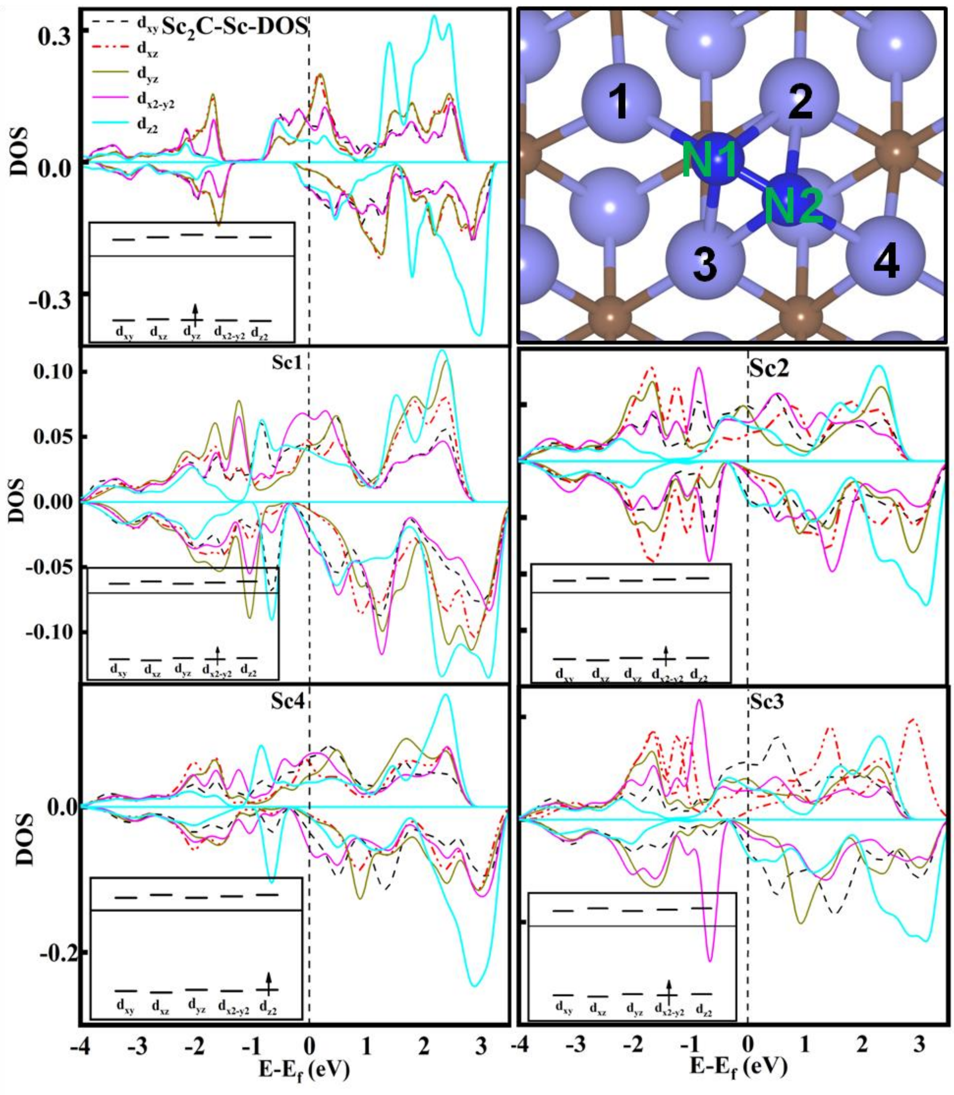

Figure S13 Spin-resolved LDOS comparison between 3*d* spin splitting for Sc on pristine Sc_2C and four Sc atoms binding to the adsorbed N-N atoms. The inset presents the corresponding electron arrangement on the spin-split *d* orbitals.

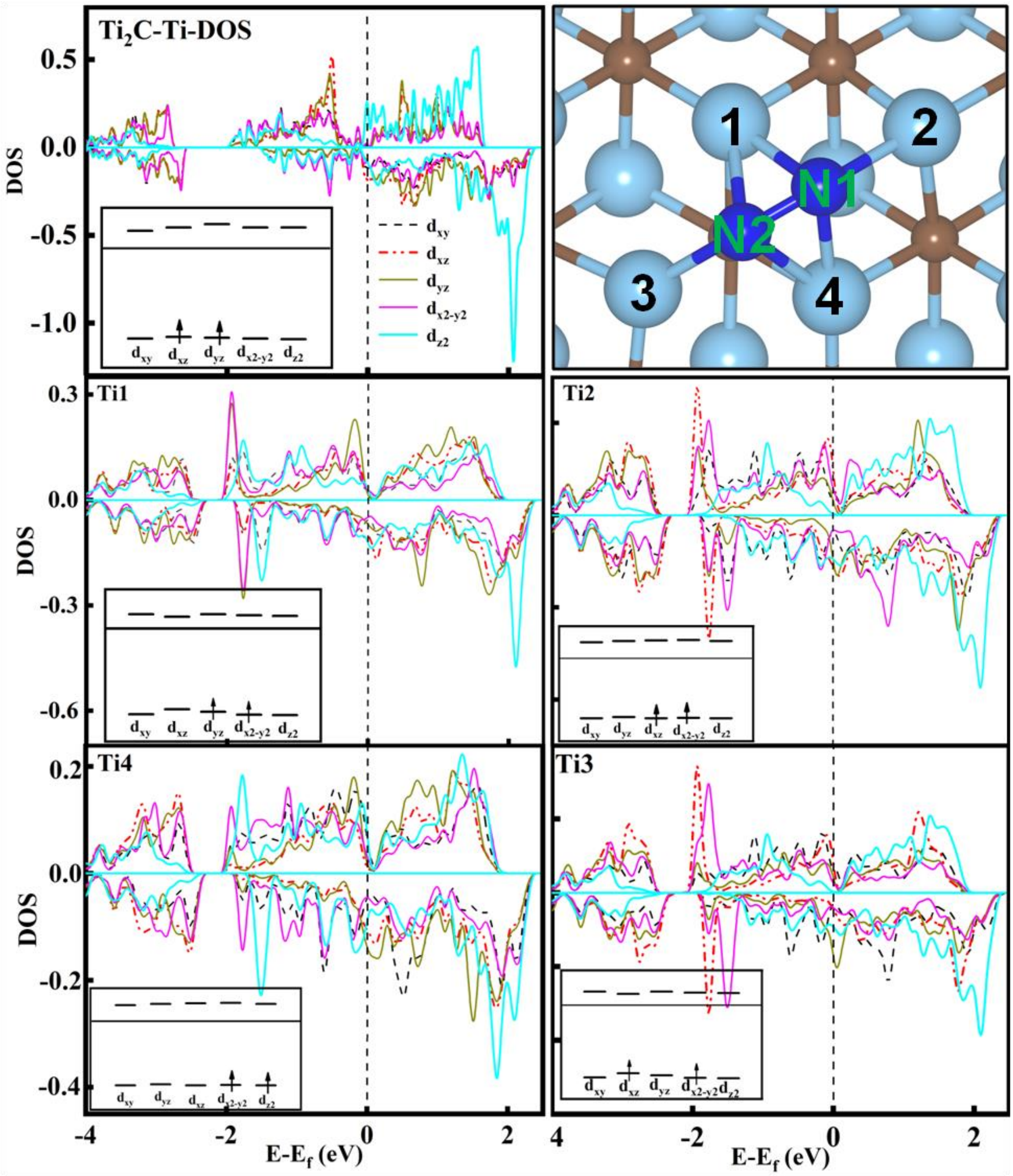

Figure S14 Spin-resolved LDOS comparison between 3*d* spin splitting for Ti on pristine Ti_2C and four Ti atoms binding to the adsorbed N-N atoms. The inset of each DOS presents the corresponding electron arrangement on the spin-split *d* orbitals.

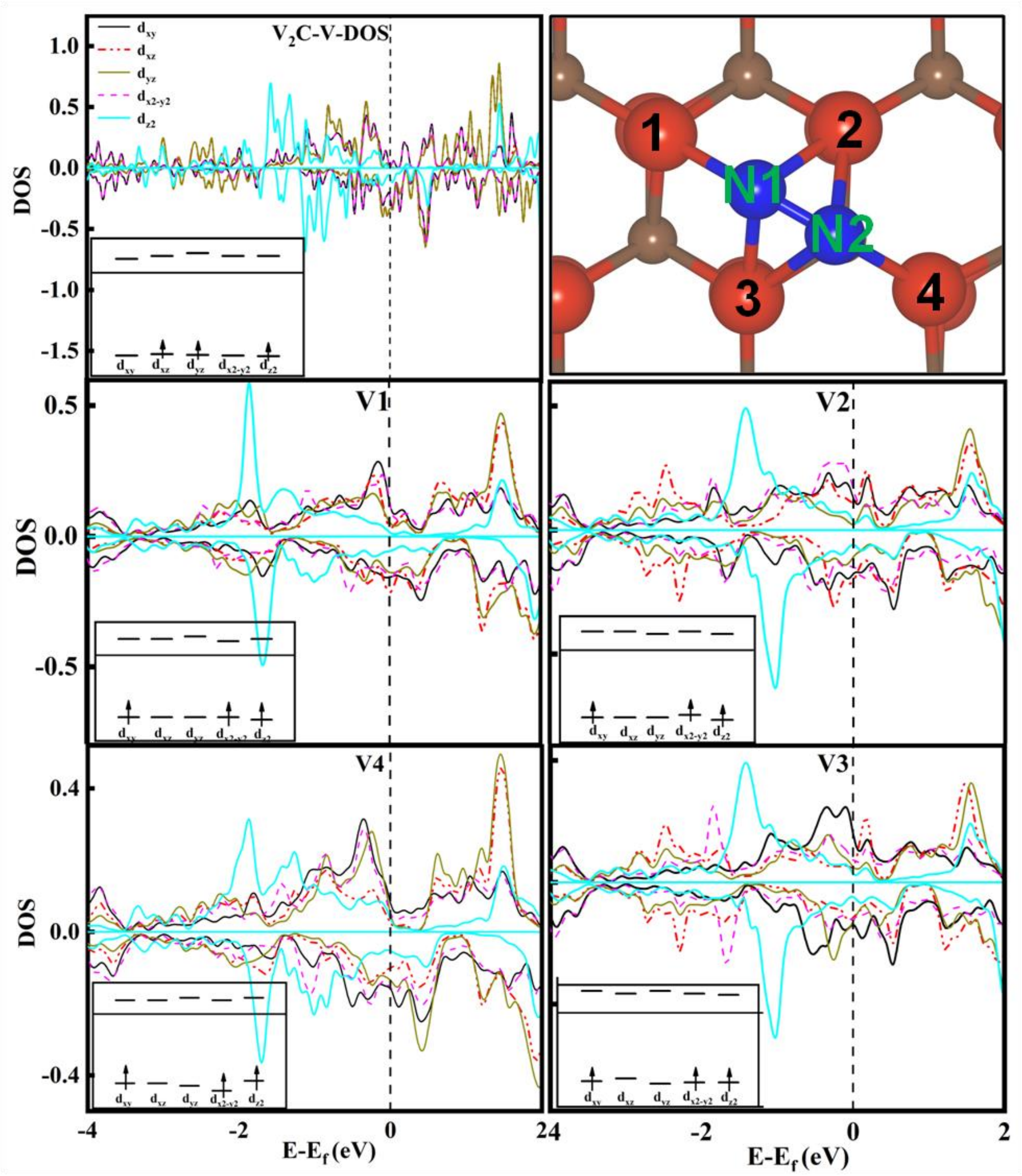

Figure S15 Spin-resolved LDOS comparison between 3*d* spin splitting for V on pristine V_2C and four V atoms binding to the adsorbed N-N atoms. The inset of each DOS presents the corresponding electron arrangement on the spin-split *d* orbitals.

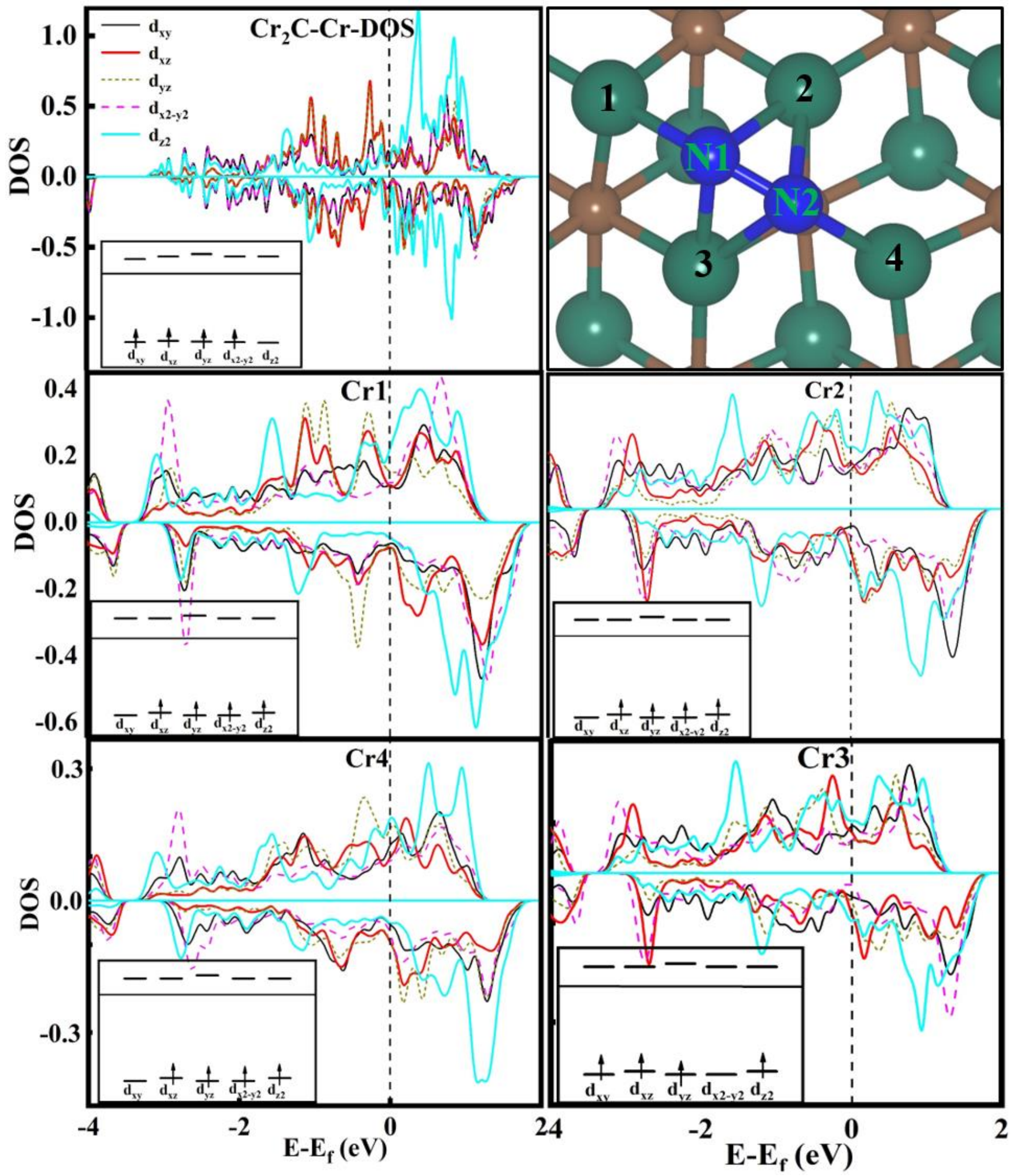

Figure S16 Spin-resolved LDOS comparison between 3*d* spin splitting for Cr on pristine Cr$_2$C and four Cr atoms binding to the adsorbed N-N atoms. The inset of each DOS presents the corresponding electron arrangement on the spin-split *d* orbitals.

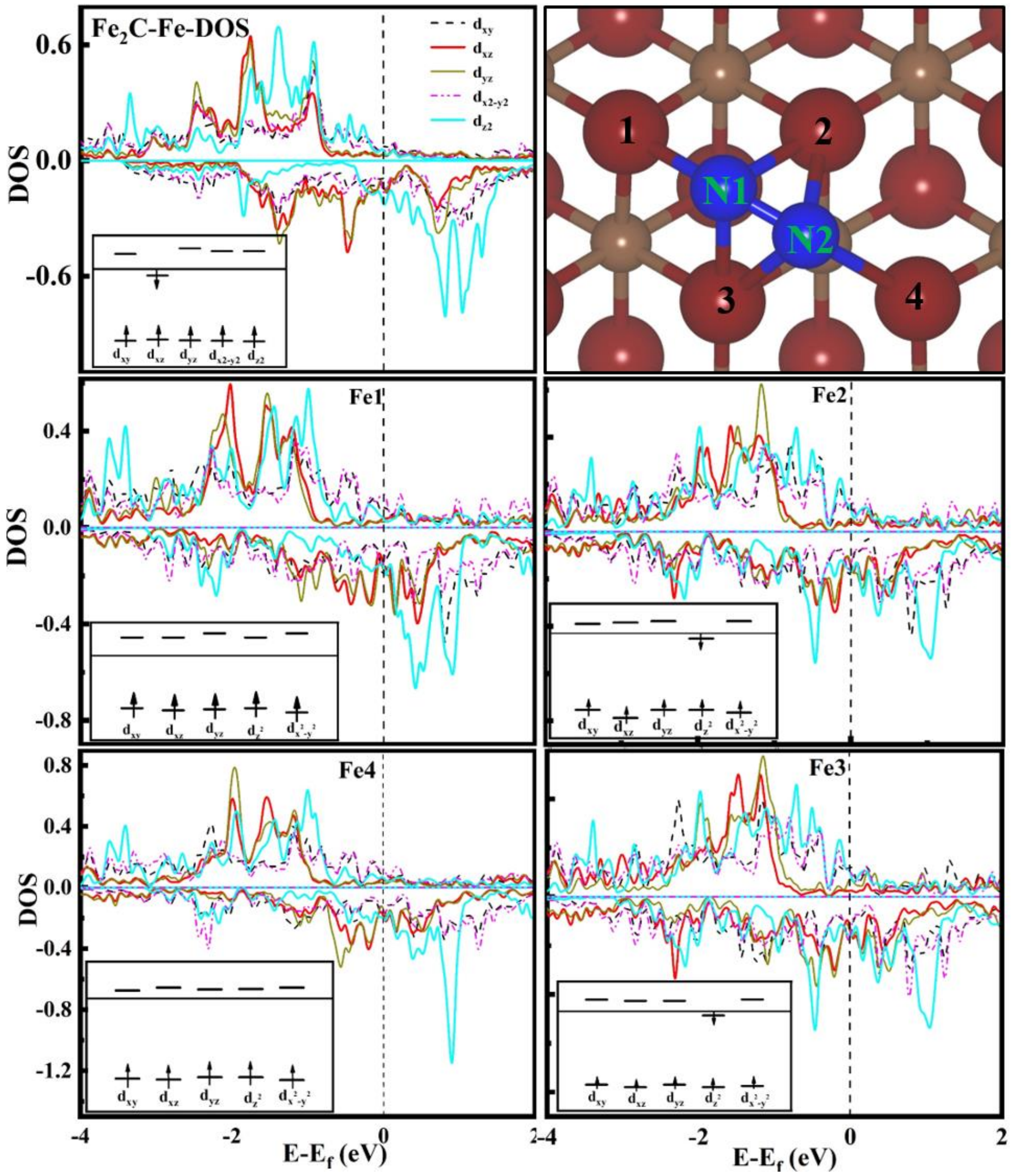

Figure 17 Spin-resolved LDOS comparison between 3*d* spin splitting for Fe on pristine Fe_2C and four Fe atoms binding to the adsorbed N-N atoms. The inset of each DOS presents the corresponding electron arrangement on the spin-split *d* orbitals.

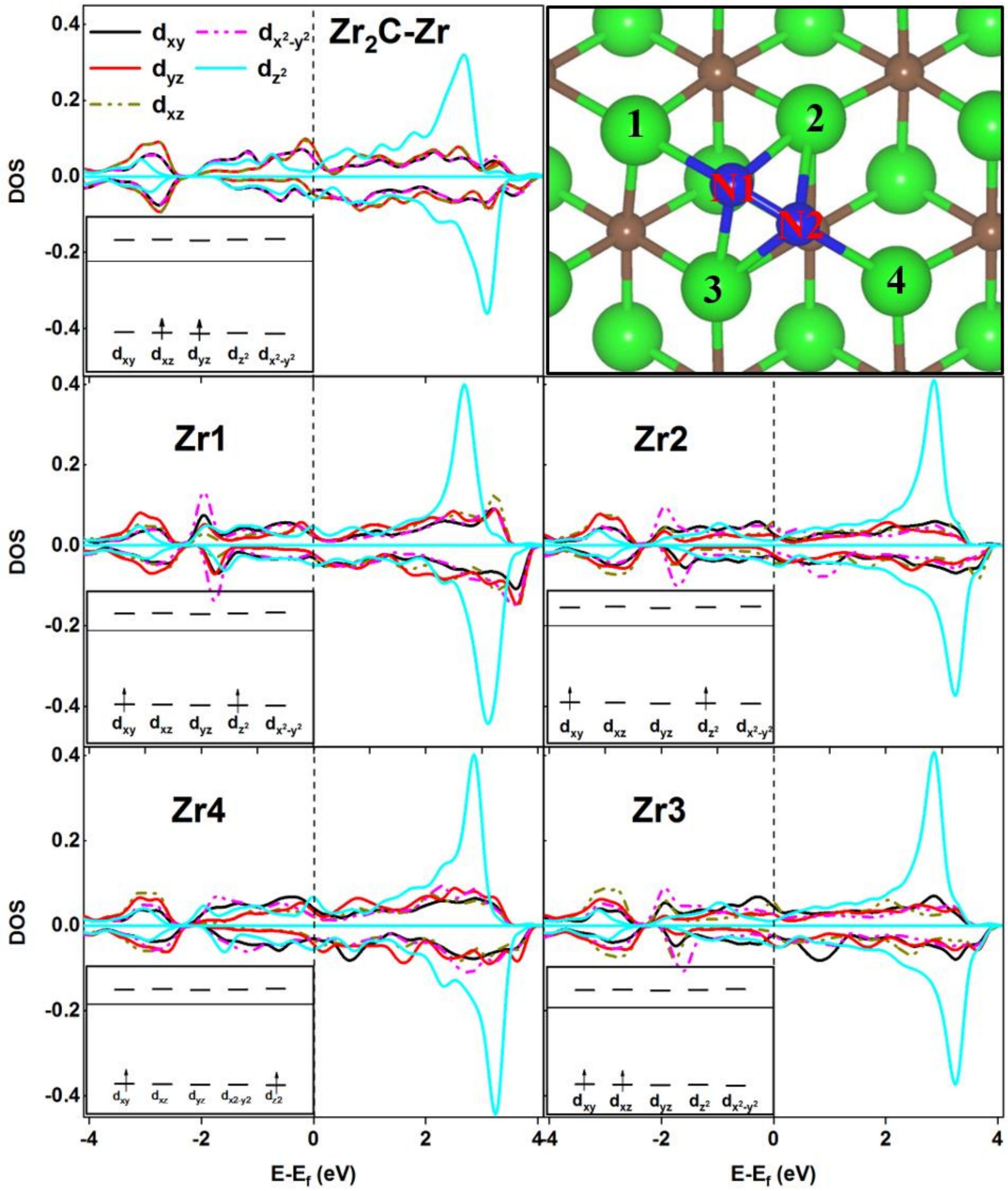

Figure 18 Spin-resolved LDOS comparison between 4*d* spin splitting for Zr on pristine Zr_2C and four Zr atoms binding to the adsorbed N-N atoms. The inset of each DOS presents the corresponding electron arrangement on the spin-split *d* orbitals.

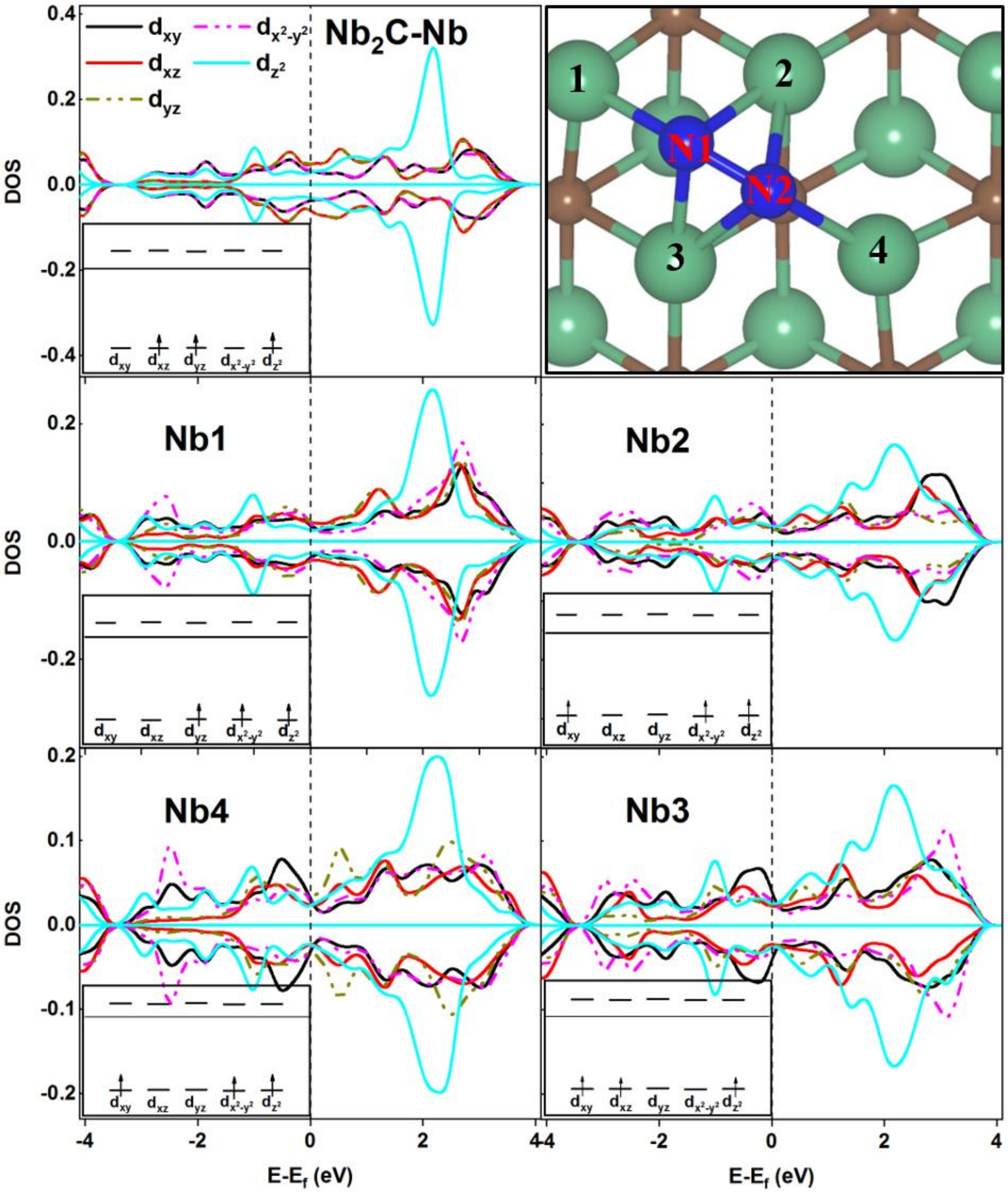

Figure 19 Spin-resolved LDOS comparison between 4*d* spin splitting for Nb on pristine Nb$_2$C and four Nb atoms binding to the adsorbed N-N atoms. The inset of each DOS presents the corresponding electron arrangement on the spin-split *d* orbitals.

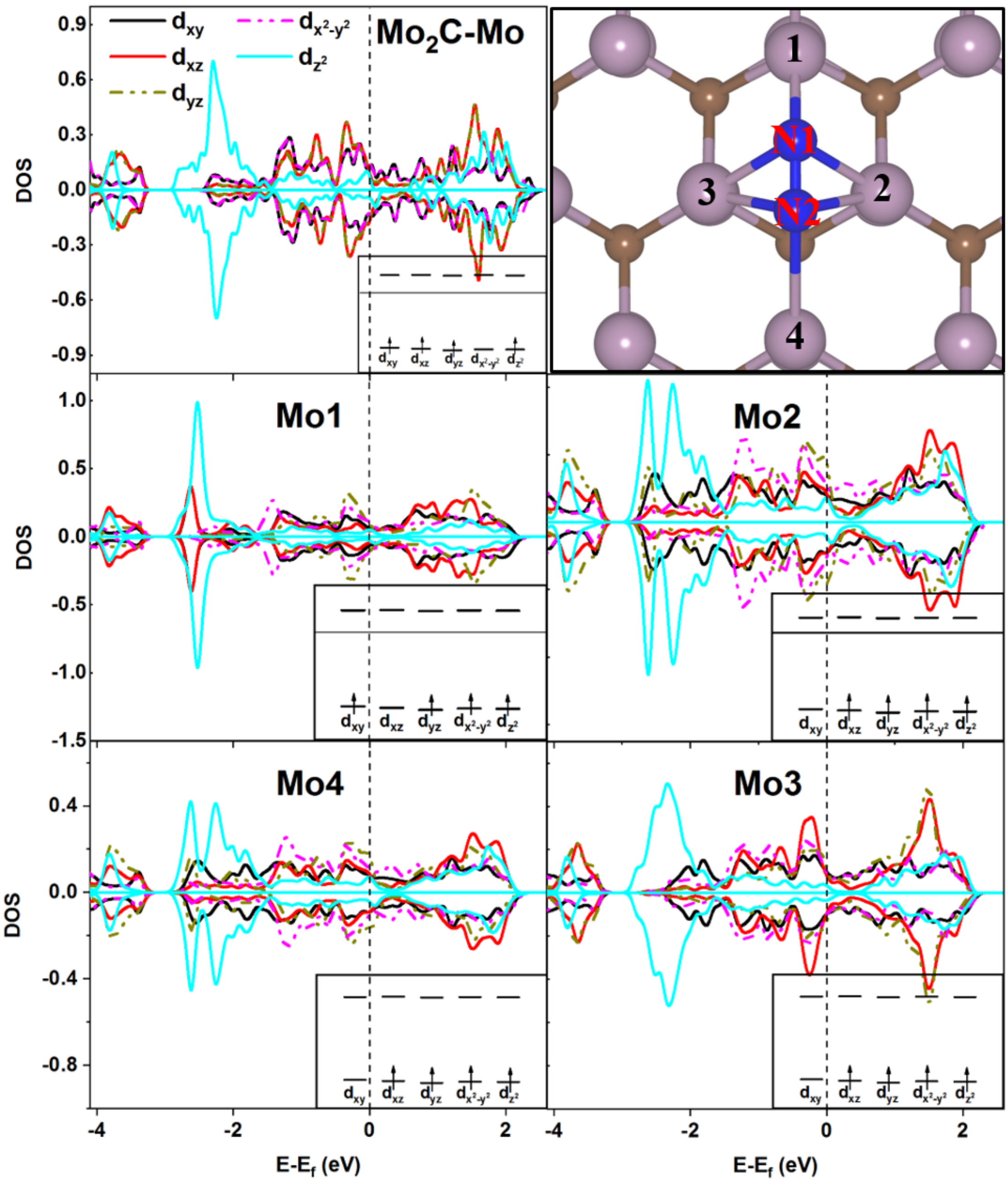

Figure 20 Spin-resolved LDOS comparison between 4*d* spin splitting for Mo on pristine Mo$_2$C and four Mo atoms binding to the adsorbed N-N atoms. The inset of each DOS presents the corresponding electron arrangement on the spin-split *d* orbitals.

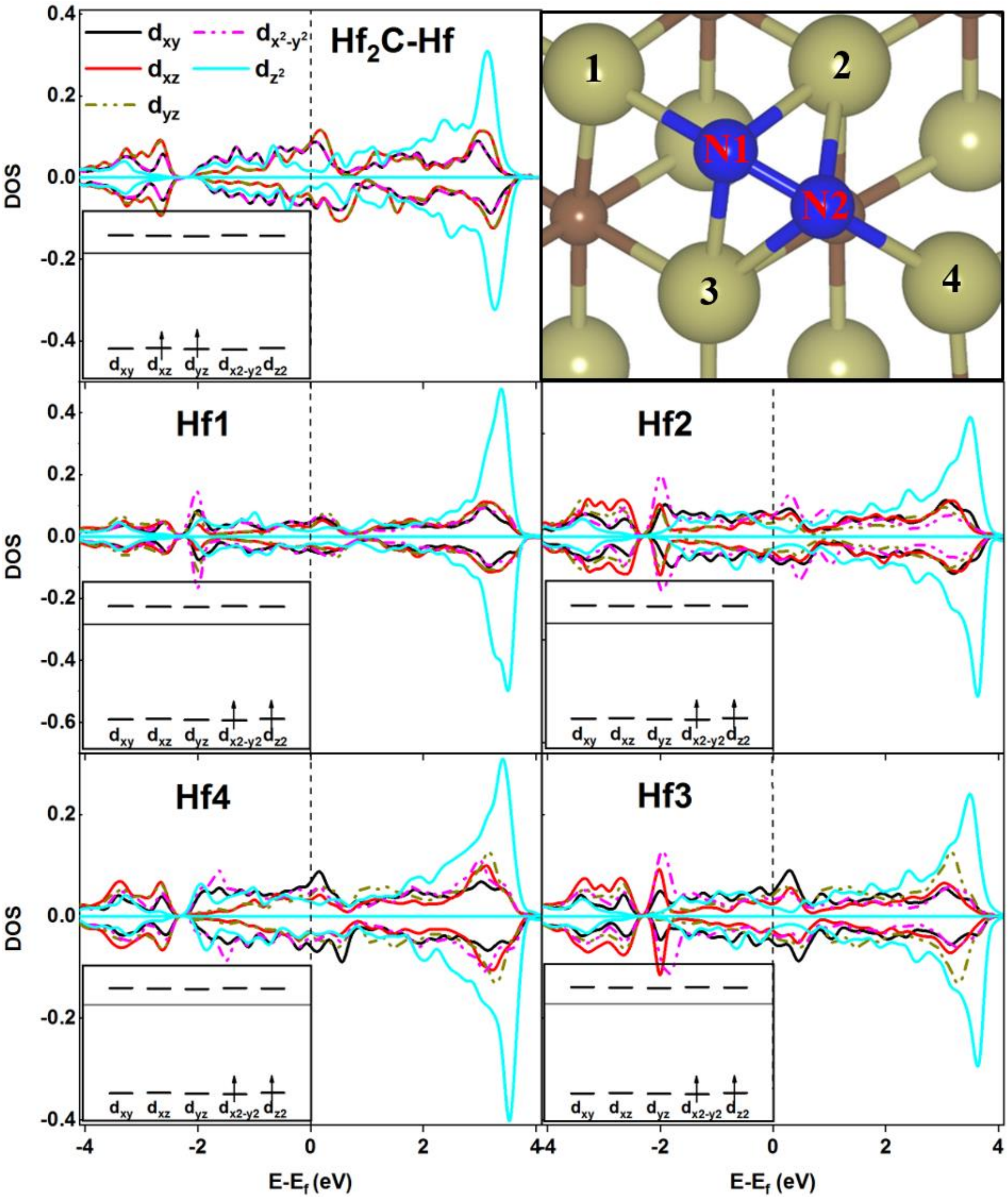

Figure 21 Spin-resolved LDOS comparison between 5*d* spin splitting for Hf on pristine Hf$_2$C and four Hf atoms binding to the adsorbed N-N atoms. The inset of each DOS presents the corresponding electron arrangement on the spin-split *d* orbitals.

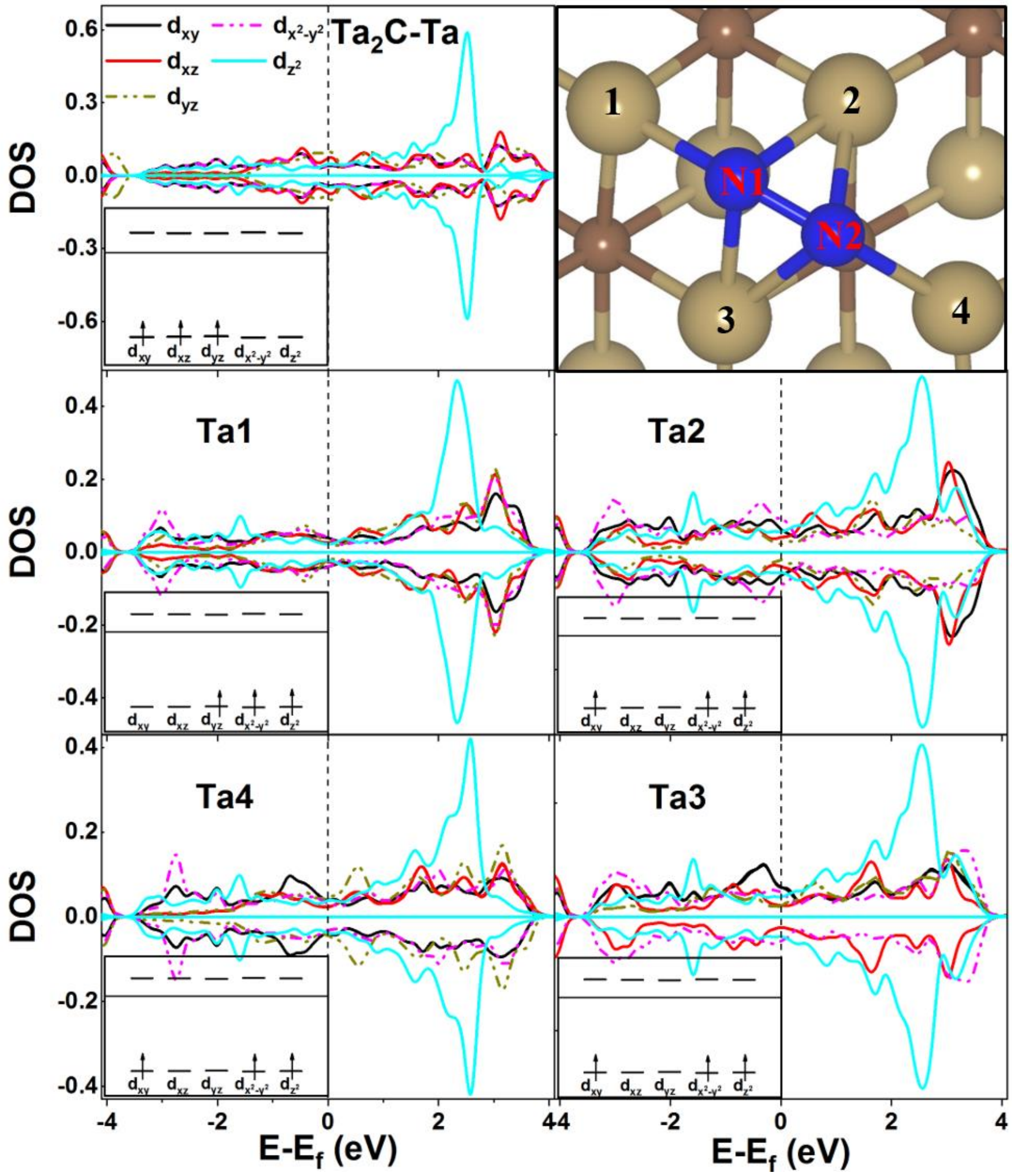

Figure 22 Spin-resolved LDOS comparison between 5*d* spin splitting for Ta on pristine Ta$_2$C and four Ta atoms binding to the adsorbed N-N atoms. The inset of each DOS presents the corresponding electron arrangement on the spin-split *d* orbitals.

Supplementary References

1. Skulason, E.; Bligaard, T.; Gudmundsdottir, S.; Studt, F.; Rossmeisl, J.; Abild-Pedersen, F.; Vegge, T.; Jonsson, H.; Norskov, J. K., A Theoretical Evaluation of Possible Transition Metal Electro-catalysts for N_2 Reduction. *Phys. Chem. Chem. Phys.* **2012,** *14* (3), 1235-1245.
2. Guo, H.; Li, L.; Wang, X.; Yao, G.; Yu, H.; Tian, Z.; Li, B.; Chen, L., Theoretical Investigation on the Single Transition-Metal Atom-Decorated Defective MoS2 for Electrocatalytic Ammonia Synthesis. *ACS Appl Mater Interfaces* **2019,** *11* (40), 36506-36514.
3. Ling, C.; Niu, X.; Li, Q.; Du, A.; Wang, J., Metal-Free Single Atom Catalyst for N_2 Fixation Driven by Visible Light. *J. Am. Chem. Soc.* **2018,** *140* (43), 14161-14168.
4. Chen, X.; Zhao, X.; Kong, Z.; Ong, W. J.; Li, N., Unravelling the Electrochemical Mechanisms for Nitrogen Fixation on Single Transition Metal Atoms Embedded in Defective Graphitic Carbon Nitride. *J. Mater. Chem. A* **2018,** *6* (44), 21941-21948.
5. Chen, Z. W.; Lang, X. Y.; Jiang, Q., Discovery of Cobweb-like MoC_6 and its Application for Nitrogen Fixation. *J. Mater. Chem. A* **2018,** *6* (20), 9623-9628.
6. Chen, Z.; Zhao, J.; Cabrera, C. R.; Chen, Z., Computational Screening of Efficient Single‐Atom Catalysts Based on Graphitic Carbon Nitride (g‐C_3N_4) for Nitrogen Electroreduction. *Small Methods* **2018,** 3, *1800368*.
7. Liu, C.; Li, Q.; Wu, C.; Zhang, J.; Jin, Y.; MacFarlane, D. R.; Sun, C., Single-Boron Catalysts for Nitrogen Reduction Reaction. *J. Am. Chem. Soc.* **2019,** *141* (7), 2884-2888.
8. Azofra, L. M.; Li, N.; MacFarlane, D. R.; Sun, C., Promising Prospects for 2D d^2–d^4 M_3C_2 Transition Metal Carbides (MXenes) in N_2 Capture and Conversion into Ammonia. *Energy Environ. Sci.* **2016,** *9* (8), 2545-2549.
9. Choi, C.; Back, S.; Kim, N.-Y.; Lim, J.; Kim, Y.-H.; Jung, Y., Suppression of Hydrogen Evolution Reaction in Electrochemical N2 Reduction Using Single-Atom Catalysts: A Computational Guideline. *ACS Catalysis* **2018,** *8* (8), 7517-7525.